

# THE EFFECT OF PLASMA ACTUATORS ON TIP CLEARANCE FLOWS IN COMPRESSOR ROTORS

A. R. Wadia\*, G. Jothiprasad\*\*, S. Saddoughi\*\*

\*GE Aviation, Cincinnati, OH, \*\*GE Global Research, Niskayuna, NY

aspi.wadia@ge.com; giridhar.jothiprasad@ge.com; saddoughi@ge.com

**Keywords:** Plasma Actuators, Transonic Compressor Rotors

## Abstract

*This paper analyzes the effect of different dielectric barrier discharge (DBD) actuator configurations on rotor tip leakage flow and stall inception in compressors. Computational investigations were performed on a low speed rotor with a highly loaded tip region that was responsible for stall-onset. The DBD was mounted on the casing upstream of the rotor leading edge. Plasma injection had a significant impact on the predicted tip-gap flow and improved stall margin. The effect of changing the actuator forcing direction on stall margin was also studied. The reduction in stalling flow was closely correlated with a reduction in loading parameter that quantifies mechanisms responsible for end-wall blockage generation. The DBD reduced end-wall losses by increasing the static pressure of tip-gap flow emerging from blade suction-side. Lastly, an approximate speed scaling developed for the DBD force helped estimate force requirements for stall margin enhancement of transonic rotors.*

## 1 Introduction

Compressor blade-tip leakage flow is a large source of loss and affects the stable operating envelope of the axial compressor [1–5]. In many cases, these detrimental effects are magnified at large tip clearance levels. The present trend in aircraft engine technology toward higher bypass ratios, to achieve lower fuel burn, has resulted in advanced compressor designs with very small blade heights, especially in the rear stages. Due to mechanical limitations on physical tip clearances that can be realistically achieved, new compressor designs

are forced to accept an increase in clearance-to-blade-height ratios from 2% to 4%. This can reduce the stall margin by nearly 50% and efficiency by 3%. Hence, there is considerable incentive to develop technologies for alleviating the stall limiting physics associated with tip clearance flows. Numerous passive casing treatments such as circumferential grooves [6,7] and skewed axial slots [8,9] have been studied in the past. However, such porous wall treatments usually result in an efficiency reduction commensurate to the stall range extension they provide [10]. Discrete tip injection technologies [11] where high momentum fluid is injected along the casing have also demonstrated potential for significant stall range increases with minimal or no loss in performance. More recently, a number of active control methodologies such as “wiggling” inlet guide vanes [12], unsteady upstream flow injection [13,14], and unsteady downstream bleed [15] have been shown to be effective in extending stable operating range of compressors. Further, technologies such as upstream flow injection have also been demonstrated [13] at transonic speeds. However, such technologies impose substantial weight penalties.

In this research the effectiveness of plasma actuation using dielectric barrier discharge (DBD) actuators for energizing the tip leakage flow and suppressing stall inception is investigated. These actuators being small and casing-mounted have minimal negative impact on the flow when not in use. Further, since there are no moving parts, these actuators are easy to maintain and have small response times (typically less than a millisecond and is critical for active feedback stall control applications).

Computational Fluid Dynamic (CFD) simulations of multiple casing actuator configurations at both low and transonic speeds were performed. The results were analyzed to better understand physical mechanisms for stall inception and force requirements for control.

Vo computationally assessed the use of DBD actuators for suppression of short-length scale (spike) stall inception in a low speed [16] and transonic [17] axial compressor. His studies suggested that the casing plasma actuator should be placed immediately upstream of the rotor leading edge to optimize the impact on the tip clearance flow. In this paper, the actuator was mounted on the casing upstream of the rotor leading edge and the effect of changing the forcing direction of the DBD actuator was studied with a low speed compressor rotor. Formulation by Shyy et al. [18] was used to model the DBD actuator forcing in a 3D Reynolds averaged Navier–Stokes [RANS] solver developed in-house for turbomachinery simulations. Changes in the tip clearance flow and losses in the tip region are presented. The reduction in stalling flow as a function of relevant non-dimensional parameters characterizing the tip flow is studied for three different actuator configurations. Next, the numerical study was extended to transonic speeds based on estimates of force requirements for stall enhancement developed using the low speed analysis. Results for the NASA Rotor 37, a well-studied axial transonic compressor, are presented.

## 2 Numerical Approach

A 3D RANS solver developed in-house is used for the turbomachinery simulations. The solver is based on the cell-centered finite volume methods of Jameson [19]. Artificial dissipation is introduced to maintain numerical stability [20]. The artificial dissipation is a blend of second and fourth differences with coefficients that depend on the local pressure gradient. Artificial dissipation levels are set to the lowest levels needed for numerical stability; the impact on the solution is minimal. A robust multigrid algorithm is used to accelerate convergence to the time steady state. The  $k-w$

turbulence model by Wilcox [21] is used for all steady-state RANS calculations. The Durbin limiter helped avoid spurious turbulence production in regions of high normal strain rates, such as the stagnation point.

The DBD actuator forcing was incorporated into this RANS solver. The DBD consists of two offset electrodes separated by a dielectric material. When an AC voltage is applied across the electrodes, a weakly ionized, low temperature, and non-thermal plasma is formed above the buried electrode. The charged particles are subjected to a force in the presence of the electric field created by the electrodes and this forcing induces flow around the exposed electrode. Since the plasma-generation kinetics occurs at much smaller lengths and times compared with the flow, only a steady body force over the ionized region is introduced in the current simulations. Wei-Shy's model [18] is used to model this body force over the region of the plasma. The small protrusion of the exposed electrode is neglected in the CFD simulations.

Lastly, a criterion is needed to identify the stalling mass flow. Different criteria [22,23] have been proposed in the past. In this research, a simple criterion based on the total-to-static pressure  $\psi_{t-s}$  is used

$$\psi_{t-s} = \frac{P_{S_2} - P_{TA_1}}{\frac{1}{2}\rho U_t^2} \quad (1)$$

where  $P_{TA_1}$  is the inlet absolute total pressure,  $P_{S_2}$  is the exit static pressure,  $\rho$  is an average flow density, and  $U_t$  is the rotor tip velocity. Stalling mass flow rate, based on linear stability arguments, is taken to be the location of maximum total-to-static pressure ratio.

## 3 Results for Low Speed Rotor

The low speed research compressor (LSRC) has 54 blades with a casing radius of 0.762 m and hub-to-tip radius ratio of 0.85. The axial chord  $c$  and solidity  $\sigma$  at the tip are 0.071m and 1.33, respectively. At the design speed, the rotor tip velocity  $U_t$  is 63.3 m/s. The numerical

study was carried out at a tip clearance gap  $g$  of 3.14% of axial chord (or 2.51% of blade-height).

### 3.1 Experimental Comparisons

The numerical simulations were validated with experimental investigations performed at the GE low speed research compressor test facility. The rotor geometry used for this validation was slightly different from that used to study actuator effectiveness. The research compressor was set up with four identical stages and detailed measurements were taken on the third stage. Static pressure loadings as well as radial profiles of total pressure, velocity components, and flow angles were measured upstream and downstream of the third stage rotor. Descriptions of the measurement systems and data reduction techniques can be found in Ref. [24].

Care was taken to ensure that the numerical simulations matched the operating conditions in the experiment. At the rotor inlet, a steady 2D non-reflective boundary condition (based on the Giles [25] formulation) was used to prescribe circumferentially averaged total temperature, total pressure, and absolute radial and tangential flow angles. At the exit, a static pressure profile is provided. The shape of the profile is held fixed while the values are varied to match a target exit mass flow. Figure 1 shows the radial variation in normalized rotor exit pressures at design and near stall operation. Both absolute total and static pressures are normalized by the total pressure at mid span. At the design operating condition, the numerical results closely match the experimental data while minor differences are observed near stall. Self-excited unsteadiness has been observed in tip clearance flows near stall. Hence, the accuracy of CFD predictions near stall can further be improved with unsteady computations [26]. However, steady RANS was used for all calculations presented in this paper. Detailed validation of this RANS solver can also be found in Ref. [26].

### 3.2 Axial Forcing

In the first actuator configuration investigated, the electrodes are oriented to produce a downstream axial force, as shown in Fig. 2. The actuator is positioned upstream of the rotor leading edge at an axial distance of 7% of the axial tip chord. Previous numerical simulations by Vo [16] have shown this configuration to be most effective in stall suppression at low rotor speeds. An axial force of 0.26 N/m is applied which is within the capability of actuators available today [17].

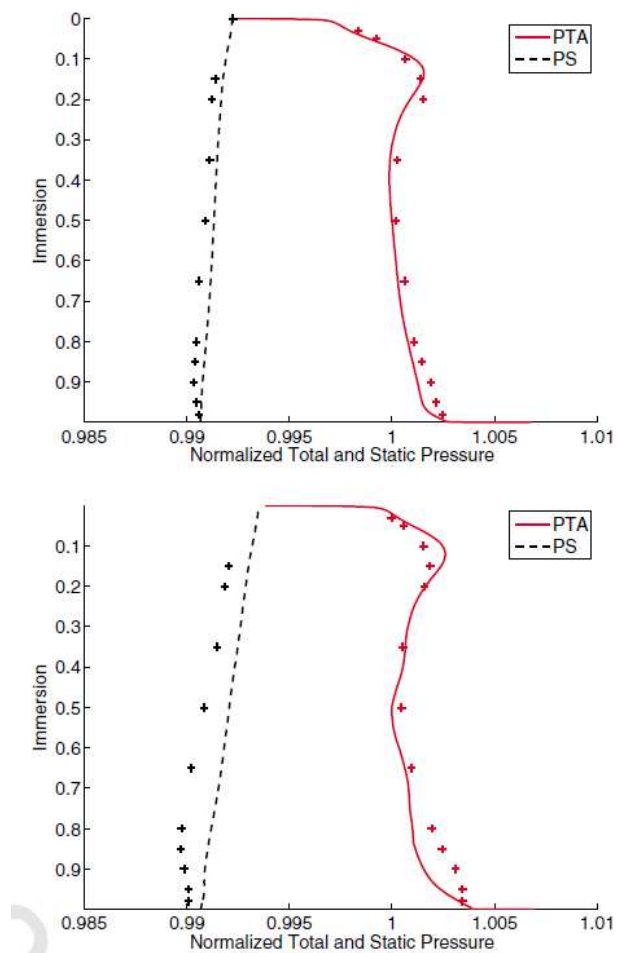
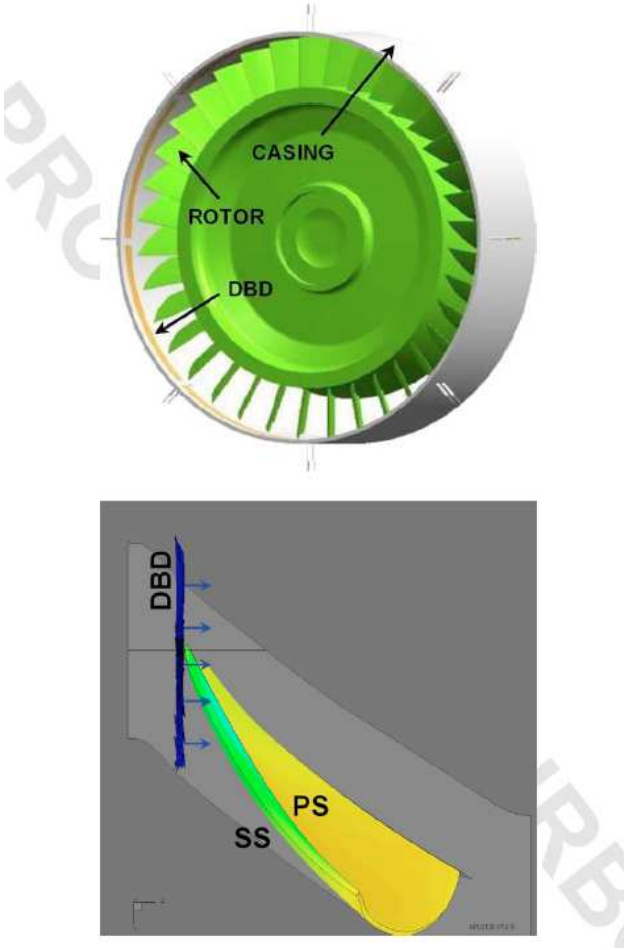


Figure 1. Radial variation in normalized rotor exit pressures. Total pressure at mid span used for normalization.



**Figure 2. DBD actuator configuration for axial downstream force. (a) Circumferential electrodes (in brown) are axially offset. (b) Forcing region and direction in blue.**

The calculated total pressure-rise characteristics with and without actuation are shown in Fig. 3. The flow coefficient  $\phi$  and total pressure-rise coefficient  $\psi$  are defined as

$$\phi = \frac{V_{x1}}{U_1} = \frac{m_1}{\rho A_1 U_1} \quad (2)$$

$$\psi = \frac{P_{TA2} - P_{TA1}}{\frac{1}{2} \rho U_1^2} \quad (3)$$

where 1 and 2 denote rotor inlet and outlet stations,  $V_{x1}$  is the mass-averaged axial velocity at rotor inlet,  $P_{TA}$  is the absolute total pressure,  $\rho$  is the average flow density,  $A_1$  is the inlet annulus area between casing and hub, and  $m_1$  is

the inlet mass flow rate. The coefficients are further normalized by the values at the baseline stall flow without actuation. Figure 3 shows that the flow coefficient at numerical stall is reduced and that the rotor operates at higher pressure ratios before stall. To quantify this increase in stall margin, the normalized change in stalling flow coefficient  $\Delta\phi_{st}$ , as defined by Suder [11], is used.

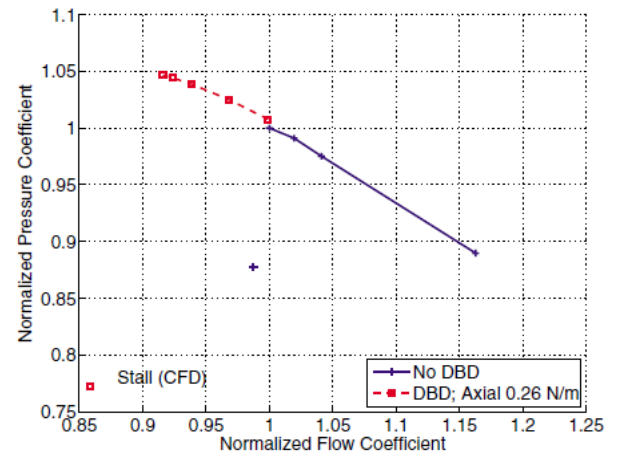


**Figure 3. Total pressure-rise coefficient as a function of flow coefficient for downstream axial force of 0.26 N/m in low speed rotor. Stalled operating points (from CFD) not connected by lines. Coefficients normalized by values at baseline stall flow.**

$$\Delta\phi_{st} = \frac{\phi_{st_b} - \phi_{st}}{\phi_{st_b}} \quad (4)$$

where  $st$  denotes operating conditions at numerical stall and  $b$  denotes baseline performance without casing actuation. For the axial forcing configuration, the stalling flow is reduced by 7.6%.

To illustrate the effect of the actuation on the tip leakage flow, Fig. 4 compares the relative total pressure losses introduced in the tip region with and without actuation. The interaction of the tip clearance vortex with the main flow creates a region of low speed fluid and high losses. In Fig. 4, the tip vortex is a region of high loss. The actuation injects momentum into the casing flow thereby energizing the tip leakage flow and causing the

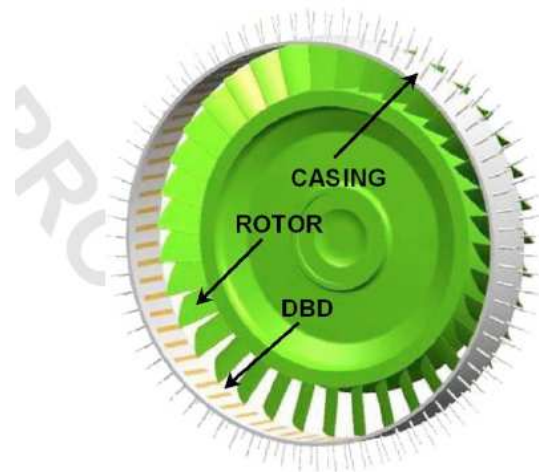
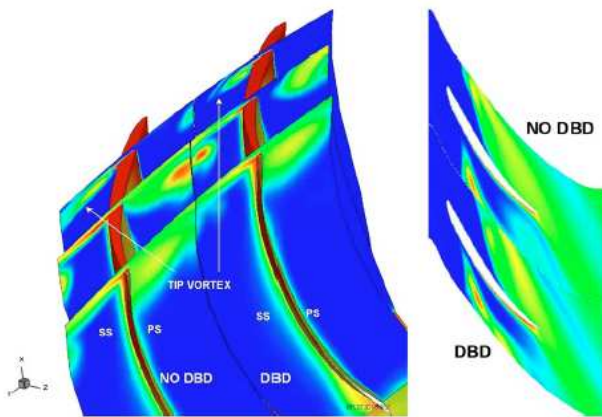


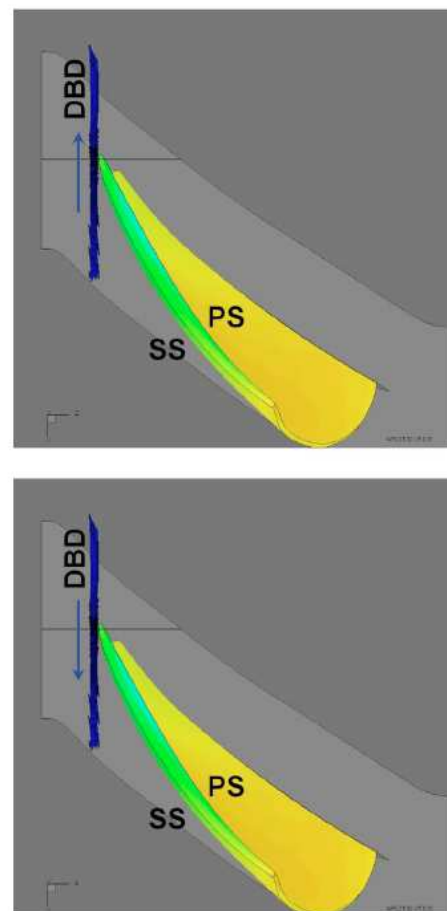
**Figure 4. Contours of non-dimensional total pressure loss with and without actuation. Comparison at baseline stall flow. Red denotes region of high loss Actuation reduces tip leakage loss.**

tip leakage vortex to be closer to the blade suction surface. This reduces the losses introduced by the tip leakage flow and increased the adiabatic efficiency by nearly 0.4% at the baseline stall flow.

### 3.3 Forcing Angle Effects

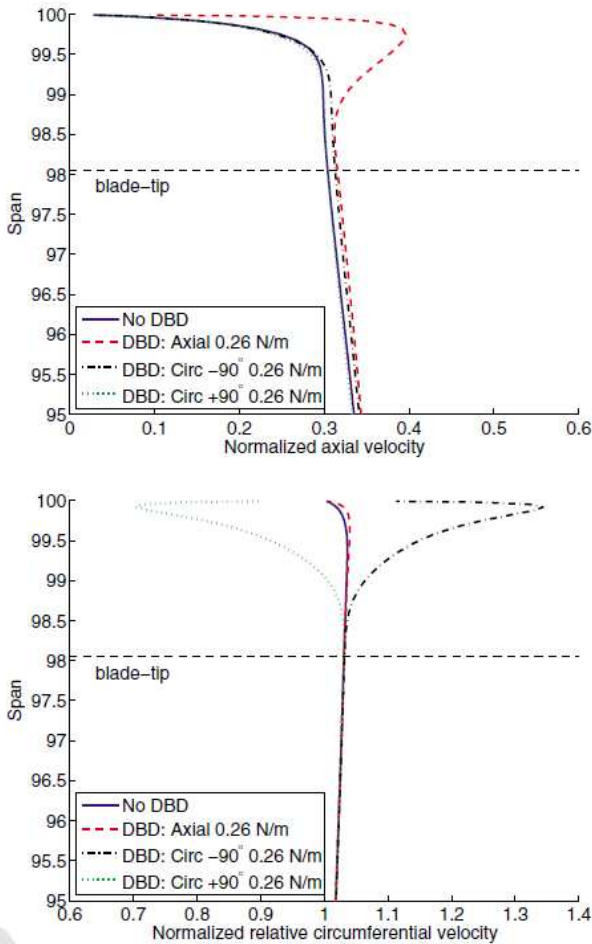
The effect of changing the forcing direction of the DBD actuator studied herein is similar to past research [27,28] on discrete tip injection that has highlighted the impact of injection angle on compressor stability improvement. In experiments, the offset of electrodes needs to be aligned normal to the desired forcing direction. Hence, using axial electrodes, as shown in Fig. 5, can produce a circumferential force. To simplify the setup of numerical simulations, only the forcing direction but not the spatial distribution of plasma forces is modified. The tested configurations include a swirl force in the blade rotation direction (denoted by circ +90 deg) and a counter-swirl opposite to the blade rotation direction (denoted by circ -90 deg).

Figure 6 compares the spanwise variation in circumferentially mass-averaged relative inlet velocities for the different DBD actuation configurations at the baseline stalling flow coefficient  $\Phi_{stb}$ . Due to momentum injection,



**Figure 5. DBD actuator configuration for circumferential force. (a) Axial electrodes (in brown) are circumferentially offset. (b) Circumferential force in direction of blade rotation. (c) Circumferential force opposite to the direction of blade rotation. Forcing region and direction in blue.**

the axial forcing increases the axial velocity near the casing while the circ +90 deg and circ -90 deg forcing modify the circumferential velocity. Also, the plasma actuation primarily affects the velocities in the region above the blade-tip.



**Figure 6. Spanwise variation of rotor inlet velocity in the blade-tip region of low speed rotor. Comparison with baseline stall flow. Velocities normalized by blade-tip speed.**

Figure 7 compares the total pressure-rise characteristics for the different actuator configurations. Both axial and circ -90 deg (counter-swirl) forcing configurations are favorable to stall margin enhancement. Interestingly, the circ +90 deg (swirl) configuration is detrimental to stall margin enhancement. Based on velocity triangles, forcing the flow in the direction of blade rotation reduces the flow incidence angle at the

blade-tip. However, the ineffectiveness of this configuration indicates that reduction in tip incidence angle is not essential to stall margin improvement of the low speed rotor.

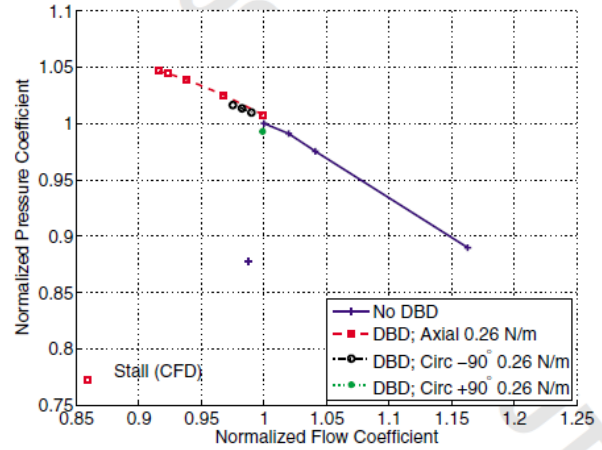


**Figure 7. Effect of varying forcing angles on total pressure-rise characteristic of low speed rotor. 0.26 N/m of force applied. Stalled operating points (from CFD) not connected by lines. Coefficients normalized by values at baseline stall flow.**

This observation is consistent with past parametric studies that varied injection angles for discrete tip injection [27,28]. Both researchers concluded that the optimum injection angle for injection is opposite to blade rotation. Similarly, experiments [29] on skewed slot casing treatments provide evidence that greatest range extension is obtained when the slots are skewed opposite to the rotor rotation. Figure 8 compares the spanwise variation in rotor incidence angles for the different DBD actuation configurations at the baseline stalling flow coefficient  $\Phi_{stb}$ . Incidence angle changes are most prominent in the region above the blade-tip while the blade operates at similar incidence angles with and without actuation. This is because the actuation primarily affects the velocities near the casing. Thus, DBD actuation enhances stability through mechanisms other than incidence angle modification.

One possible explanation for the stability enhancement is that favorable actuator configurations unload the blade-tip region. The highly loaded tip region in the current rotor is

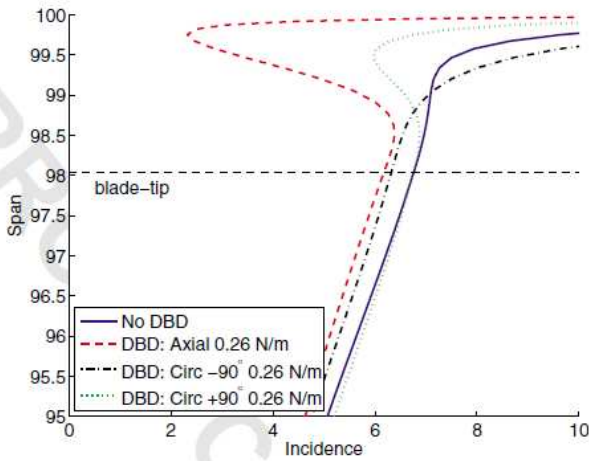


**Figure 8. Spanwise variation in rotor incidence angles in the blade-tip of low speed rotor. Comparison at baseline stall flow.**

primarily responsible for blockage growth and onset of stall. Hence, reducing the blade-tip loading allows stable compressor operation at lower mass flow rates. The circumferentially averaged diffusion factor has been widely used [10,11,27,28] to quantify blade loading

$$DF(\%span \text{ from hub}) = 1.0 - \frac{W_2}{W_1} + \frac{W_{\theta_2} - W_{\theta_1}}{2\sigma W_1} \quad (5)$$

where stations 1 and 2 are roughly 2% axial chord upstream of the rotor leading edge and 2% axial chord downstream of the rotor trailing edge, respectively,  $W$  is the circumferentially mass averaged relative total velocity, and  $W_\theta$  is the circumferentially mass-averaged relative circumferential velocity. Prior experimental [11,30] and numerical [28] results have shown that stability enhancement technologies like tip injection lower the blade diffusion factor at the tip. Figure 9 compares the diffusion factor at the baseline stalling flow coefficient  $\Phi_{stb}$  for the different DBD actuation configurations. This figure confirmed that the favorable axial and circ  $-90$  deg forcing reduced the diffusion factor near the blade-tip. Further, the circ  $+90$  deg forcing increased the blade-tip diffusion factor and hence was detrimental to stall margin enhancement.

Another plausible explanation is that the plasma actuation energizes the casing boundary

layer in the relative frame of reference. The diffusion factor measures blade loading based on the airfoil suction surface diffusion process. However, stall is also likely to occur when casing wall boundary layers grow to a limiting value when subject to a maximum static pressure rise [31]. To characterize the ability of the casing boundary layer to withstand an adverse pressure gradient, the static pressure rise across the rotor is normalized by the relative dynamic head

$$\psi_S(\%span \text{ from hub}) = \frac{P_{S_2} - P_{S_1}}{\frac{1}{2}\rho W_1^2} \quad (6)$$

where  $P_S$  is the circumferentially mass-averaged static pressure.

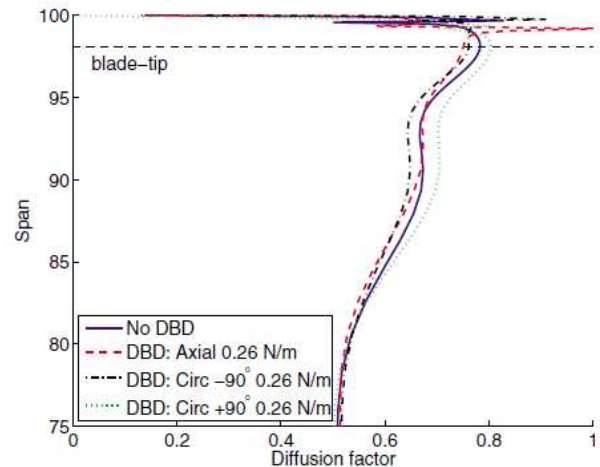


**Figure 9. Spanwise variation in diffusion factor in the blade-tip region of low speed rotor. Comparison of DBD configurations at baseline stall flow. Favorable configurations unload blade-tip region.**

Figure 10 plots the variation in static-pressure-rise coefficient near the blade-tip. There are dramatic reductions for the favorable actuator configurations and hence the rotor stalls at higher pressure ratios and lower flow rates.

The blade-tip diffusion factor and static-pressure-rise coefficient allow favorable actuator configurations to be identified. However, the reduction in stalling flow is not

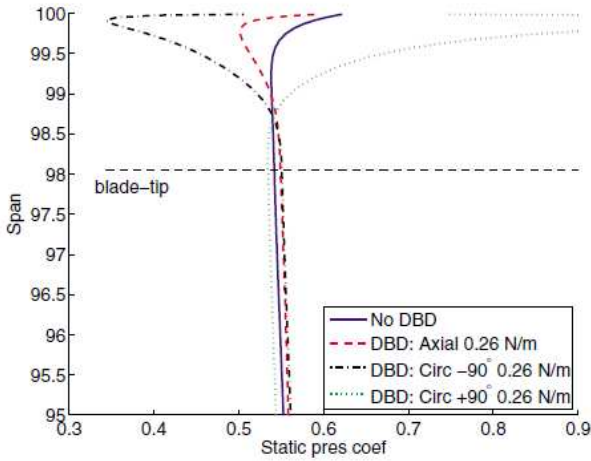


**Figure 10. Spanwise variation in static-pressure-rise coefficient in the blade tip region of low speed rotor. Comparison of DBD configurations at baseline stall. Static pressure rise across the blade is normalized by inlet relative velocity.**

proportional to the reduction in either diffusion factor or static-pressure-rise coefficient. Even though the circ  $-90^\circ$  deg forcing is most effective in energizing the casing boundary layer (Fig. 10), the axial forcing results in a larger stalling flow decrease (Fig. 7). Similarly, the reductions in blade-tip diffusion factor for axial and circ  $-90^\circ$  deg forcing are comparable (see Fig. 9) while the stall margin improvement for the two configurations are very different (Fig. 7). Hence, another parameter that captures the interaction of tip leakage flow with the main passage flow is investigated.

### 3.4 End-Wall Blockage

The early work by Koch and Smith [31,32] identified the relationship between the blockage generated in the compressor and its pressure-rise and operating flow range. Khalid et al. [33] later presented a methodology for quantifying the end-wall blockage that provides physical insight into the flow features responsible for blockage generation. Khalid et al. developed a correlation between the end-wall blockage and a loading parameter based on static pressure gradient and losses experienced by the tip clearance flow. Furthermore, computations and

experiments by Khalid and others [33,34] have identified a limiting value for this loading parameter.

Research by Khalid et al. describes a simplified end-wall blockage generation mechanism for compressors. The mixing of tip clearance flow with freestream results in relative total pressure loss and associated blockage generation. Furthermore, this initial tip blockage grows when the tip flow is subject to a strong static pressure rise until it reaches the rotor exit plane. The loading parameter  $CP_S-CP_T$  captures the contribution of these two mechanisms to blockage creation at the tip. It is computed by mass-averaging a local loading parameter over the tip clearance flow emerging above the blade suction-side tip. The local loading parameter as defined by Khalid et al. is  $(CP_S-CP_T)_{loc}$  where

$$(CP_S)_{loc} = \frac{\langle P_{S_{exit}} \rangle_a - P_{S_{loc,ss}}}{P_{T_{ref,1}} - P_{S_{loc,ss}}} \quad (7)$$

and

$$(CP_T)_{loc} = \frac{\langle P_{T_{exit}} \rangle_a - P_{T_{ref,1}}}{P_{T_{ref,1}} - P_{S_{loc,ss}}} \quad (8)$$

$CP_T$  represents the relative total pressure loss of tip flow,  $CP_S$  represents the static pressure rise experienced by the tip flow,  $(\bullet)_a$  denotes area-averaging over the blocked region at the blade-row exit near casing,  $(\bullet)_{loc,ss}$  denotes a local value in the tip gap region above the blade suction surface, and  $(\bullet)_{ref,1}$  denotes circumferentially area-averaged flow variables at the inlet station over a region that is approximately two tip gaps from the casing wall. The blocked region at the blade-row exit is identified using Khalid's algorithm [33,34]. Figure 11 depicts the blocked region computed for the low speed rotor at the baseline stalling flow coefficient. End-wall blockage due to the tip vortex accumulates on the pressure-side blade-surface.  $(\bullet)_a$  is computed by limiting the area average to the blocked region in the 10% span near casing wall.

Figure 12 shows the reduction in stalling flow with the loading parameter computed at the baseline stalling flow coefficient  $\Phi_{stb}$ . Results from different actuator forcing angles and forcing strengths are presented. It can be seen that the reduction in stalling flow is well

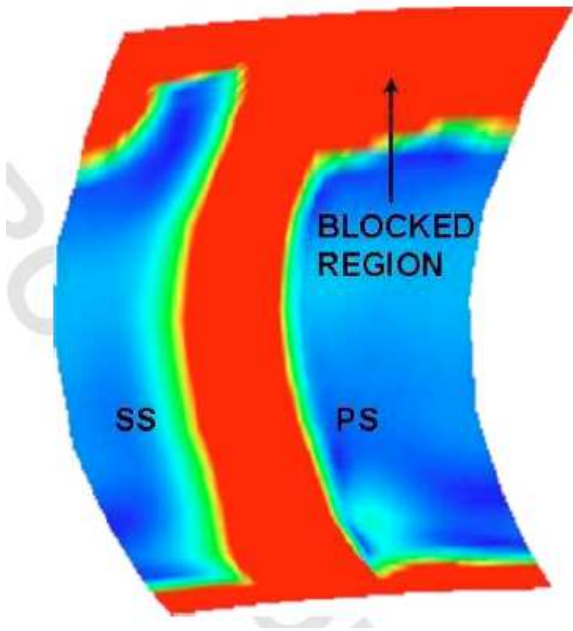


Figure 11. Blocked region (in red) at exit plane of low speed rotor. Exit blockage due to wakes and tip vortex.

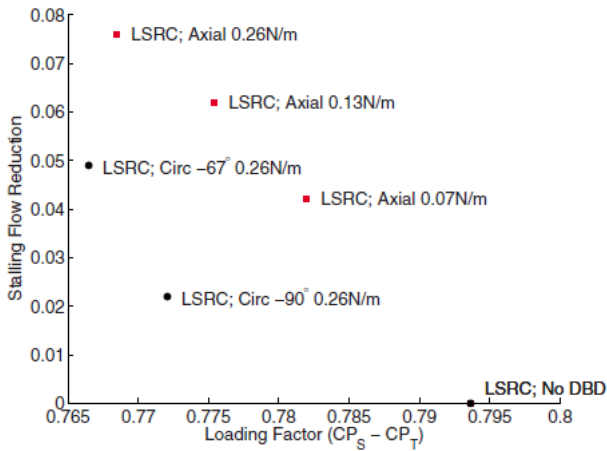


Figure 12. Reduction in stalling flow  $\Delta\Phi_{st}$  with loading parameter  $CP_S - CP_T$  at baseline stall flow.

correlated with a decrease in loading parameter due to actuation. Among the forcing angles tested, the axial forcing was most effective in reducing loading parameter and hence in reducing stalling flow. Lastly, the variation in DBD forcing strength for the axial configuration shows that the stall flow reduction is almost linear with DBD forcing strength.

The original definition of the loading parameter (Eqs. (7) and (8)) uses the inlet relative total pressure to compute the local dynamic head of the tip clearance flow. This definition allows both experimental and numerical results to be processed in a similar fashion. However, it is assumed that the flow through the clearance gap experiences almost no loss and there is no double leakage of fluid from one clearance gap into the adjacent blade's tip gap. Figure 13 shows that the radially averaged relative total pressure at the tip gap varies significantly from the leading to the trailing edge of the low speed rotor. This is primarily due to double leakage of fluid from the adjacent blade-row. Hence, the definition of loading parameter is modified as follows:

$$(CP'_S)_{loc} = \frac{\langle P_{S_{exit}} \rangle_a - P_{S_{loc,ss}}}{P_{T_{loc,ss}} - P_{S_{loc,ss}}} \quad (9)$$

and

$$(CP'_T)_{loc} = \frac{\langle P_{T_{exit}} \rangle_a - P_{T_{ref,l}}}{P_{T_{loc,ss}} - P_{S_{loc,ss}}} \quad (10)$$

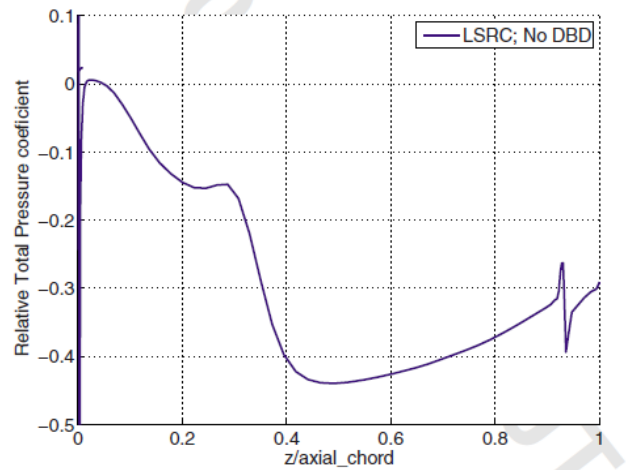


Figure 13. Variation in radially averaged relative total pressure at the tip gap with axial distance.

Figure 14 shows the reduction in stalling flow with the modified loading parameter computed at the baseline stalling flow coefficient  $\Phi_{stb}$ . Again, the stalling flow reduction is well correlated with the decrease in modified loading parameter due to actuation. Figure 14(a) indicates that the stalling flow is

#### 4 Transonic Rotor Results

Motivated by the stall margin enhancement observed at low speeds, the effectiveness of DBD actuation was researched at transonic speeds. NASA Rotor 37, a well-studied axial transonic compressor [35], was chosen for the following investigation. This rotor was used as the test vehicle for the ASME sponsored “blind test-case study” for CFD [36]. The rotor has 36 blades with a casing radius of 0.254 m and hub-to-tip radius ratio of 0.70. The axial chord  $c$  and solidity at the tip are 0.028 m and 1.288, respectively. At the design speed, the rotor tip velocity  $Ut$  is 447.62 m/s. The numerical study was carried out at a tip clearance gap  $g$  of 2.56% of axial chord (or 0.88% of blade-height). The experimentally measured tip gap was doubled to increase the influence of tip clearance flow on rotor stall.

A non-dimensional scaling for the actuation force is obtained to estimate the actuation force required for stall enhancement at transonic speeds. Low-speed results highlighted the importance of reducing the loading parameter which scales with the dynamic head of the tip clearance flow  $(P_T - P_S)_{loc,ss}$ . Hence, an appropriate scaling for the DBD forcing is

$$F^* = \frac{F \times s}{(P_T - P_S)_{ref,1} \times g \times c} \quad (11)$$

where  $F^*$  and  $F$  denote the non-dimensional and dimensional DBD force/unit length, and  $s$  denotes the stagger gap. The numerator is a measure of the DBD force applied at the casing over an entire blade passage and the denominator is a measure of the relative dynamic head of the flow through the tip clearance gap. Table 1 summarizes the non-dimensional forcing and the corresponding stalling flow reduction for the tested configurations in the low speed simulations.

Based purely on the above scaling arguments, it is estimated that an axial force of 5.24 N/m is required for reducing the stalling flow by 7.6%. However, these scaling arguments may fail at transonic speeds because

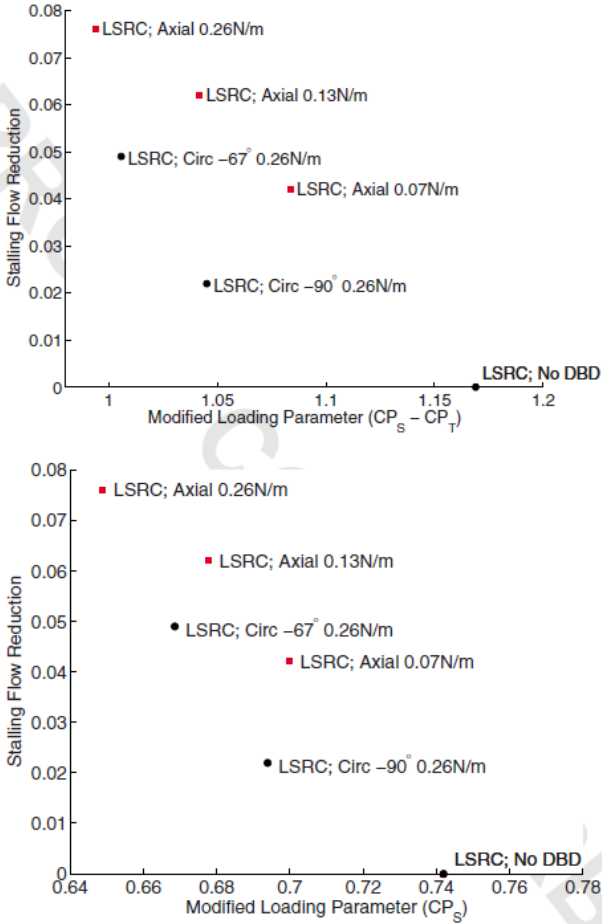


**Figure 14. Reduction in stalling flow  $\Delta\Phi_{st}$  with (a) modified loading parameter ( $CP'_S - CP'_T$ ) at baseline stall flow. (b) Static pressure rise  $CP'_S$  of tip flow.**

reduced through a reduction of both the static-pressure-rise of tip flow and the total pressure loss of mixing. Nearly 70% of the contribution to the loading parameter is from the static-pressure-rise at tip  $CP'_S$ . Hence, the effect of reducing static-pressure-rise  $CP'_S$  at the tip is isolated in Fig. 14(b). Among the non-dimensional parameters investigated, the stalling flow reduction for the low speed rotor is closely correlated with a decrease in  $CP'_S$ . Thus, the DBD actuation reduces the end-wall blockage and losses by increasing the static pressure of the tip clearance flow emerging from the blade suction-side. This allows tip critical rotors to operate at lower mass flow rates before stalling.

Table 1 Reduction of stalling flow  $\Delta\phi_{st}$  with dimensional  $F$  and nondimensional  $F^*$  forcing for the low speed rotor

Forcing angle	$F$ (N/m)	$F^*$	$\Delta\phi_{st}$ (%)
Axial	0.07	0.008	4.2
Axial	0.13	0.015	6.2
Axial	0.26	0.031	7.6
Circ (-90 deg)	0.26	0.031	2.2
Circ (-67 deg)	0.26	0.031	4.9

physical mechanisms not present at low speeds such as shock-vortex interaction may govern the stalling behavior of the rotor. Hence, to ensure that the stall margin is enhanced, the simulations were carried out using an increased DBD force of 8.63 N/m and 17.26 N/m. Today’s DBD actuators cannot produce such large forces. Hence, the CFD simulations are essentially a numerical experiment to better understand force requirements or stall enhancement at transonic speeds.

The calculated total pressure-rise characteristics with and without actuation are shown in Fig. 15.

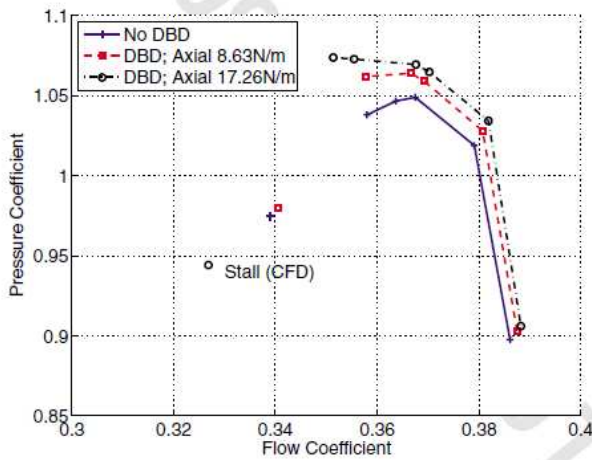


Figure 15. Total pressure rise coefficient as a function of flow coefficient for two levels of axial forcing in the transonic NASA Rotor 37. Stalled operating points not connected by lines.

At the stable operating conditions, the rotor operates at a higher flow and pressure coefficient when the casing actuation is applied. The increase in flow coefficient is due to a reduction in end-wall blockage and loss. Figure 15 also indicates a lowering of the stalling flow

coefficient with casing actuation. Preliminary analysis indicates that this decrease is not commensurate with that observed at low speeds. However, there is a significant increase in total pressure-rise coefficient near stall due to improved end-wall flow. Vo et al. [17] had observed similar behavior in numerical simulations for the transonic NDS01 rotor with casing DBD actuation, although Vo et al. had not observed a decrease in stalling flow. This is probably due to the much lower DBD forcing used (-1.2 N/m). It is not clear whether different speed scaling arguments were used for his choice of forcing strength.

In summary, the casing DBD actuation reduces end-wall losses at transonic speeds. NASA Rotor 37 results indicate that casing actuation increases the total pressure-rise coefficient near stall and marginally decreases the stalling flow.

## 5 Concluding Remarks

The effectiveness of plasma actuation for affecting tip clearance flows and suppressing stall inception was studied numerically at low and transonic rotor speeds. Wei-Shy’s model for steady DBD forcing was incorporated into a 3D Reynolds averaged Navier–Stokes solver developed for turbomachinery simulation. The actuator was positioned on the casing upstream of the rotor leading edge. Results for three different forcing directions in a low speed compressor rotor were presented. Relevant non-dimensional parameters to characterize tip flows and stall margin improvement were investigated. Lastly, the force requirement of actuation at transonic speeds was studied using the NASA Rotor 37 as a test-case. Some specific findings were the following.

1. DBD actuation reduced the end-wall blockage and losses by energizing the tip leakage flow and increasing the static pressure of the tip clearance flow emerging from the blade suction-side.
2. Among the actuator configurations tested at low speeds, the axial and circ -90 deg (counter-swirl) forcing configurations were favorable to stall margin enhancement.

3. Ineffectiveness of circ +90 deg forcing configuration indicated that reduction in tip incidence angle was not essential to stall margin improvement of the low speed rotor.
4. Qualitatively, blade loading at the tip and ability of casing boundary layer to withstand static-pressure-rise, represented by diffusion factor and static-pressure-rise coefficient, respectively, were both reduced for favorable actuator configurations. However, quantitatively, the reduction in stalling flow was not proportional to the reduction in either factor.
5. Khalid's loading parameter captured the contribution of two mechanisms to blockage generation: static pressure rise of tip flow and total pressure loss of mixing. The stalling flow reduction for the low speed rotor was well correlated with the reduction in loading parameter.
6. Among the non-dimensional parameters investigated, the stalling flow reduction for the low speed rotor was closely correlated with a decrease in static pressure rise of tip flow  $CP'_s$ .
7. An approximate non-dimensional speed scaling to estimate the DBD force required at transonic speeds was developed. The required DBD force scales with the relative dynamic head of the flow through the tip clearance gap.
8. For the transonic compressor, NASA Rotor 37, casing actuation increased total pressure-rise coefficient near stall by reducing end-wall losses. The stalling flow was marginally decreased but this decrease is not commensurate with that observed at low speeds.

## References

- [1] Cumpsty, N., 1989, *Compressor Aerodynamics*, Krieger, Malabar, FL, Chap. 9, pp. 359–409.
- [2] Storer, J. A., and Cumpsty, N. A., 1991, "Tip Leakage Flow in Axial Compressors," *ASME J. Turbomach.*, **113**(2), pp. 252–259.
- [3] Storer, J. A., and Cumpsty, N. A., 1994, "An Approximate Analysis and Prediction Method for Tip Clearance Loss in Axial Compressors," *ASME J. Turbomach.*, **116**(4), pp. 648–656.
- [4] Wadia, A. R., 1985, "Numerical Solution of Two- and Three-Dimensional Rotor Tip Leakage Flows," *AIAA J.*, **23**(7), pp. 1061–1069.
- [5] Hah, C., Rabe, D. C., and Wadia, A. R., 2004, "Role of Tip-Leakage Vortices and Passage Shock in Stall Inception in a Swept Transonic Compressor Rotor," *ASME Paper No. GT2004-53867*.
- [6] Prince, D., Wisler, D., and Hilver, D., 1974, "Study of Casing Treatment Stall Margin Improvement Phenomena," NASA Technical Report No. CR-134552.
- [7] Shabbir, A., and Adamczyk, J. J., 2005, "Flow Mechanism for Stall Margin Improvement Due to Circumferential Casing Grooves on Axial Compressors." *ASME J. Turbomach.*, **127**(4), pp. 708–717.
- [8] Johnson, M. C., and Greitzer, E. M., 1987, "Effects of Slotted Hub and Casing Treatments on Compressor Endwall Flow Fields," *ASME J. Turbomach.*, **109**(3), pp. 380–387.
- [9] Smith, G. D. J., and Cumpsty, N. A., 1984, "Flow Phenomena in Compressor Casing Treatment," *ASME J. Eng. Gas Turbines Power*, **106**(3), pp. 532–541.
- [10] Hathaway, M. D., 2006, "Passive Endwall Treatments for Enhancing Stability," NASA Technical Report No. NASA/TM-2007-214409.
- [11] Suder, K. L., Hathaway, M. D., Thorp, S. A., Strazisar, A. J., and Bright, M. B., 2001, "Compressor Stability Enhancement Using Discrete Tip Injection," *ASME J. Turbomach.*, **123**(1), pp. 14–23.
- [12] Paduano, J. D., Epstein, A. H., Valavani, L., Longley, J. P., Greitzer, E. M., and Guenette, G. R., 1993, "Active Control of Rotating Stall in a Low-Speed Axial Compressor," *ASME J. Turbomach.*, **115**(1), pp. 48–56.
- [13] Weigl, H. J., Paduano, J. D., Frechette, L. G., Epstein, A. H., Greitzer, E. M., Bright, M. M., and Strazisar, A. J., 1998, "Active Stabilization of Rotating Stall and Surge in a Transonic Single Stage Axial Compressor," *ASME J. Turbomach.*, **120**, pp. 625–636.
- [14] Spakovszky, Z. S., Weigl, H. J., Paduano, J. D., van Schalkwyk, C. M., Suder, K. L., and Bright, M. M., 1999, "Rotating Stall Control in a High-Speed Stage With Inlet Distortion: Part I—Radial Distortion," *ASME J. Turbomach.*, **121**, pp. 510–516.
- [15] Koch, C. C., and Smith, L. H., Jr., 1968, "Experimental Evaluation of Outer Casing Blowing or Bleeding of Single Stage Axial Flow Compressor, Part IV—Performance of Bleed Insert Configuration No. 3," NASA Technical Report No. CR-54590.
- [16] Vo, H. D., 2007, "Suppression of Short Length-Scale Rotating Stall Inception With Glow Discharge Actuation," *ASME Paper No. GT2007-27673*.
- [17] Vo, H. D., Cameron, J. D., and Moris, S. C., 2008, "Control of Short Length-Scale Rotating Stall Inception on a High-Speed Axial Compressor With Plasma Actuation," *ASME Paper No. GT2008-50967*.
- [18] Shyy, W., Jayaraman, B., and Anderson, A., 2002, "Modeling of Glow Discharge-Induced Fluid Dynamics," *J. Appl. Phys.*, **92**(11), pp. 6434–6443.
- [19] Jameson, A., 1983, "Solution of the Euler Equations for Two Dimensional Transonic Flow by a Multigrid Method," *Appl. Math. Comput.*, **13**, pp. 327–355.
- [20] Jameson, A., Schmidt, W., and Turkel, E., 1981, "Numerical Solution of the Euler Equations by Finite Volume Methods Using Runge-Kutta Time Stepping Schemes," 14th Fluid and Plasma Dynamics Conference, Paper No. 1259, AIAA.
- [21] Wilcox, D., 1993, *Turbulence Modeling for CFD*, DCW Industries, La Canada, CA.

- [22] Vo, H. D., Tan, C. S., and Greitzer, E. M., 2008, "Criteria for Spike Initiated Rotating Stall," *ASME J. Turbomach.*, **130**, p. 011023.
- [23] Hynes, T. P., and Greitzer, E. M., 1987, "A Method for Assessing Effects of Circumferential Flow Distortion on Compressor Stability," *ASME J. Turbomach.*, **109**(3), pp. 371–379.
- [24] Wisler, D. C., Halstead, D. E., and Beacher, B. F., 1999, "Improving Compressor and Turbine Performance Through Cost Effective Low-Speed Testing," 14th International Symposium on Air Breathing Engines, Paper No. ISABE99-7073.
- [25] Giles, M. B., 1990, "Nonreflecting Boundary Conditions for Euler Equation Calculations," *AIAA J.*, **28**(12), pp. 2050–2058.
- [26] Lee, D., Orkwis, P. D., Tsung, F.-L., Magnuszewski, W., Noll, C., and Mc-Nulty, S., 2008, "Numerical Investigation on the Effects of Self-Excited Tip Flow Unsteadiness and Blade-Row Interactions on the Performance of a Low Speed Compressor Rotor," ASME Paper No. GT2008-51385.
- [27] Cassina, G., Beheshti, B. H., Kammerer, A., and Abhari, R. S., 2007, "Parametric Study of Tip Injection in an Axial Flow Compressor Stage," ASME Paper No. GT2007-27403.
- [28] Khaleghi, H., Teixeira, J., Tousi, A., and Boroomand, M., 2008, "Parametric Study of Injection Angle Effects on Stability of Transonic Axial Compressor," *J. Propul. Power*, **24**(5), pp. 1100–1107.
- [29] Takata, H., and Tsukuda, Y., 1977, "Stall Margin Improvement by Casing Treatment—Its Mechanism and Effectiveness," *ASME J. Eng. Power*, **99**(1), pp. 121–133.
- [30] Hathaway, M. D., and Strazisar, A. J., 1998, "Impact of Discrete Tip Injection on Stabilization of a Transonic Compressor Rotor," 21st Army Science Conference.
- [31] Koch, C. C., 1981, "Stalling Pressure Rise Capability of Axial Flow Compressor Stages," *ASME J. Eng. Power*, **103**(4), pp. 645–656.
- [32] Koch, C. C., and Smith, L. H., Jr., 1976, "Loss Sources and Magnitudes in Axial-Flow Compressors," *ASME J. Eng. Power*, **98**(3), pp. 411–424.
- [33] Khalid, S. A., Khalsa, A. S., Waitz, I. A., Tan, C. S., Greitzer, E. M., Cumpsty, N. A., Adamczyk, J. J., and Marble, F. E., 1999, "Endwall Blockage in Axial Compressors," *ASME J. Turbomach.*, **121**(3), pp. 499–509.
- [34] Suder, K. L., 1998, "Blockage Development in a Transonic, Axial Compressor Rotor," *ASME J. Turbomach.*, **120**, pp. 465–476.
- [35] Moore, R. D., and Reid, L., 1980, "Performance of Single-Stage Axial Flow Transonic Compressor With Rotor and Stator Aspect Ratios of 1.19 and 1.26, Respectively, and With Design Pressure Ratio of 2.05," NASA Technical Report No. 1659.
- [36] Denton, J., 1996, "Lessons Learned From Rotor 37," Third International Symposium on Experimental and Computational Aerothermodynamics of Internal Flows (ISAIF).

## Copyright Statement

The authors confirm that they, and/or their company or organization, hold copyright on all of the original material included in this paper. The authors also confirm that they have obtained permission, from the copyright holder of any third party material included in this paper, to publish it as part of their paper. The authors confirm that they give permission, or have obtained permission from the copyright holder of this paper, for the publication and distribution of this paper as part of the ICAS2012 proceedings or as individual off-prints from the proceedings.